Photodissociation channels for N_2O near 130 nm studied by product imaging

H. M. Lambert, E. W. Davis, O. Tokel, A. A. Dixit, and P. L. Houston[a)]
Department of Chemistry and Chemical Biology, Cornell University, Ithaca, New York 14853-1301

(Received 14 December 2004; accepted 18 February 2005; published online 2 May 2005)

The photodissociation of N_2O at wavelengths near 130 nm has been investigated by velocity-mapped product imaging. In all, five dissociation channels have been detected, leading to the following products: $O(^1S)+N_2(X\,^1\Sigma)$, $N(^2D)+NO(X\,^2\Pi)$, $N(^2P)+NO(X\,^2\Pi)$, $O(^3P)+N_2(A\,^3\Sigma^+_u)$, and $O(^3P)+N_2(B\,^3\Pi_g)$. The most significant channel is to the products $O(^1S)+N_2(X^1\Sigma)$, with strong vibrational excitation in the N_2. The $O(^3P)+N_2(A,B):N(^2D,^2P)+NO$ branching ratio is measured to be 1.4 ± 0.5, while the $N_2(A)+O(^3P_J):N_2(B)+O(^3P_J)$ branching ratio is determined to be 0.84 ± 0.09. The spin-orbit distributions for the $O(^3P_J)$, $N(^2P_J)$, and $N(^2D_J)$ products were also determined. The angular distributions of the products are in qualitative agreement with excitation to the $N_2O(\tilde{D}\,^1\Sigma^+)$ state, with participation as well by the $^3\Pi_v$ state.
 [DOI: 10.1063/1.1888579]

INTRODUCTION

Nitrous oxide is an important component of the earth's natural atmosphere, produced primarily by biological processes in soils and oceans. Mostly inert in the troposphere, it is transported to the stratosphere where it is destroyed both by photodissociation and by reaction. Its mixing ratio falls from about 300 parts per 10^9 by volume (ppbv) at the tropopause to about 20 ppbv at 40 km, with a sharp decline beginning at about 25 km. This decline is partially due to the photodissociation

$$N_2O + h\nu \rightarrow N_2(X\,^1\Sigma) + O(^1D). \tag{1}$$

This process occurs at wavelengths below about 220 nm, but is most effective in the atmospheric window at about 200 nm. N_2O is also destroyed in the stratosphere by reaction with $O(^1D)$ produced either in (1) or from the dissociation of ozone

$$N_2O + O(^1D) \rightarrow N_2 + O_2 \tag{2}$$

$$\rightarrow NO + NO. \tag{3}$$

NO produced in (3) is the primary catalytic agent destroying the stratospheric ozone in the natural atmosphere, as noted by Crutzen.[1]

At shorter wavelengths, N_2O can be excited to the $C(^1\Pi)$ state near 145 nm or to the $D(^1\Sigma^+)$ state near 130 nm. The absorption coefficient for the latter transition is high,[2–4] about 80 Mb (1 Mb$=10^{-18}$ cm^2). Although the dissociation process (1) near 200 nm has been extensively studied,[5–13] that at shorter wavelengths is both more complex and less well understood. At 130 nm, the following channels are thought to be important:

$$N_2O + h\nu \rightarrow O(^1S) + N_2(X\,^1\Sigma^+_g) \tag{4}$$

$$\rightarrow N(^2D) + NO(X\,^2\Pi) \tag{5}$$

$$\rightarrow N(^2P) + NO(X\,^2\Pi) \tag{6}$$

$$\rightarrow O(^3P) + N_2(A\,^3\Sigma^+_u) \tag{7}$$

$$\rightarrow O(^3P) + N_2(B\,^3\Pi_g). \tag{8}$$

Black *et al.*[14] investigated the $O(^1S)$, $N(^2D)$, and $N_2(A\,^3\Sigma^+_u)$ products in the photodissociation of N_2O from 110 to 150 nm. While the $O(^1S)$ was detected directly from its emission at 557.7 nm, the $N(^2D)$ was detected indirectly from its reaction with N_2O to give $NO(B\,^2\Pi)$, which decays radiatively. Similarly, $N_2(A\,^3\Sigma^+_u)$ was detected indirectly from its energy transfer to NO, yielding $NO(A\,^2\Sigma^+)$, which decays radiatively. They report that the $O(^1S)$ quantum yield is near unity in the 128–138-nm range, that the $N(^2D)$ quantum yield is nearly zero at 130 nm, and that the quantum yield for $N_2(A\,^3\Sigma^+_u)$ is less than 10% at 130 nm. No information is available from these experiments on the dynamics of the dissociation, i.e., on what the kinetic energy release is for any of the channels studied.

Kinetic-energy release data is available, although at low resolution, from the experiments of Gilpin and Welge (GW)[15] and of Stone, Lawrence, and Fairchild (SLF).[16] In both studies, a molecular beam of N_2O was dissociated with a flash lamp operating near 130 nm, and the arrival time of metastable fragments at an ionizer was recorded. In the SLF study, data for the 130-nm photodissociation indicate that the vibrational distribution for the $N_2(X\,^1\Sigma)$ product extends from $v=0$ to $v=6$ with a peak at $v=3$.[16] None of the other channels was investigated. In the GW study, processes (4) and (7) were observed, but the limited resolution precluded detailed energy analysis.

a)Electronic mail: plh2@cornell.edu

A deeper understanding of the dissociation process is provided by the theoretical work of Hopper, who performed extensive multiconfiguration self-consistent-field/configuration interaction (MCSCF/CI) calculations identifying some 30 electronic states of nitrous oxide.[17] In particular, the correlation diagrams of Figs. 9 and 10 in Ref. 17 show that the $N_2O(\tilde{D}\,^1\Sigma^+)$ state reached at 130 nm correlates with dissociation channels (4) and (6), while excitation to a nearby $^3\Pi_v$ state correlates to channels (7) and (5). Channel (8) correlates with a bent geometry of the $^3\Pi_v$ state. The $\tilde{D}\,^1\Sigma^+$ state is of A′ symmetry when the molecule is bent away from a linear geometry, while the $^3\Pi_v$ state separates into two configurations, one of A′ symmetry and of A″ symmetry.

In the results described below, we have investigated channels (4)–(8) by using product imaging to detect the angular distributions for the five channels as well as the kinetic-energy release for each of the product atoms or diatoms. The atomic products were probed by resonant $(1+1')$ ionization using vacuum-ultraviolet excitation for the first step, while the diatomic products were probed by nonresonant ionization. Our work is part of a larger effort at Cornell to characterize this photodissociation process. Witinzki, Ortiz-Suárez, and Davis have used oxygen Rydberg time-of-flight spectroscopy to study channels (7) and (8), with results that are in reasonable agreement with ours.[18]

EXPERIMENT

A skimmed molecular beam of N_2O was introduced along the axis of a time-of-flight mass spectrometer (TOFMS), through the central holes in a set of three parallel, circular electrodes. Midway between the high-voltage repeller and accelerator plates, the beam was crossed at right angle by three or more copropagating laser beams. Along the intersection cylinder, the laser radiation photolyzed N_2O and ionized the recoiling dissociation products. The resulting ion cloud was accelerated through the opening in the third plate, held at ground, into a field-free region, all the while expanding at the velocities from the dissociation. The voltages and spacing of the electrodes were chosen to focus ions born with the same velocity onto a position-sensitive, dual microchannel plate assembly coupled to a fast phosphor screen at the end of the time-of-flight (TOF) tube. Gating the detector allowed a fast charge-coupled device (CCD) camera to record the resulting two-dimensional image of the ion cloud on the detector for a particular ion mass. This ion-imaging technique has been described in detail elsewhere.[19–21]

Vacuum-ultraviolet (VUV) laser radiation was used both to photodissociate N_2O and to detect the products by multiphoton ionization techniques. VUV photons were generated by a nonlinear four-wave mixing scheme at the difference frequency $(2\omega_1-\omega_2)$ between a two-photon resonance in krypton and a tunable photon in the visible to infrared region. Ultraviolet laser radiation (ω_1) at 212.55 nm $(\sim 0.8$ mJ/pulse) was employed to excite the $5p[0,1/2,0] \leftarrow\leftarrow 4p^6$ transition in Kr by frequency doubling with a beta-barium borate (BBO) crystal the output of a neodymium: yttrium aluminum garnet (Nd:YAG) (third harmonic) pumped Scanmate dye laser. The tunable (ω_2) photon employed in the VUV generation was produced by a second dye laser, pumped by the second harmonic of the same Nd:YAG laser. The ω_1 and ω_2 lasers were spatially and temporally overlapped by means of dichroic mirrors and a delay line, respectively, and focused by an achromatic lens into a stainless steel tube containing 10–20-Torr Kr. The resulting VUV and the residual incident laser light entered the TOFMS through a MgF_2 collimating lens, which served as the exit window of the Kr cell. With horizontal and vertical polarizations of ω_1 and ω_2, respectively, the resulting polarization of the VUV was vertical and parallel to the plane of the detector.

N_2O was dissociated near the peak of the absorption curve at wavelengths around 130 nm, which were convenient for detection of atomic products by $(1+1')$ resonance-enhanced multiphoton ionization (REMPI), namely, $O(^3P_{2,1,0})$ at 130.2, 130.5, and 130.6 nm and $N(^2P_{3/2})$ at 131.05 and 131.09 nm, respectively. In each case, the VUV dissociation wavelength was coincident with an atomic resonance to an excited electronic state, which could then be ionized by absorption of the residual 212.55-nm UV laser light. The detection of atomic products at dissociation wavelengths other than an atomic resonance required the generation of a second VUV wavelength. This was accomplished by sending a second visible laser into the Kr cell, coincident in time and spatially overlapped with the previously mentioned UV and visible lasers, which generated the first VUV wavelength. The scheme has been described more fully in a previous report.[22] With the photolysis laser tuned just off the $O(^3P_2)$ resonance near 130.2 nm, $N(^2D)$ and $O(^1S)$ photofragments could be detected with the second VUV laser by $(1+1')$ REMPI schemes at 124.3 and 121.76 nm, respectively. The ω_2 photons required to generate the VUV wavelengths were 578 nm for $O(^3P_2)$, 561 nm for $N(^2P)$, 731 nm for $N(^2D)$, and 835 nm for $O(^1S)$. The latter wavelength was obtained as the first Stokes line from Raman shifting 620 nm in H_2. Typical laser pulse energies were 2–5 mJ for the visible light and 1–2 mJ for the Raman-shifted infrared light.

Due to appreciable absorption by N_2O at 124.3 and 121.76 nm, product images recorded by two VUV color schemes were a composite of dissociation processes at both pump and probe wavelengths. The contribution to the dissociation at the detection wavelength was minimized by optimizing the Kr pressure for more efficient VUV generation at the dissociation wavelength. The remaining contribution at the detection wavelength was removed by a background subtraction scheme, involving the use of electronic shutters in each ω_2 laser. This allowed images to be collected on alternate sequences of laser shots, with dissociation and detection wavelengths together and then each separately.

Several experiments were undertaken with a photomultiplier tube replacing the camera and without gating the detector. The TOF mass spectra were recorded in this way for the mass peaks at N^+, O^+, N_2^+, and NO^+ as a function of the laser power for each of the ω_1 and ω_2 lasers. This was repeated for NO and N_2 gases to determine the origin of the observed molecular ions. The scans of the ω_2 laser wavelength were useful in determining the spin-orbit branching ratios by comparison of the integrated ion signals at each of

TABLE I. Product branching ratios: Spin-orbit populations and dissociation channels.

Atomic spin-orbit population ratios ($\pm 2\sigma$)	
$N(^2D_{5/2}):N(^2D_{3/2})$	1.37 ± 0.11
$N(^2P_{3/2}):N(^2P_{1/2})$	1.9
$O(^3P_2):O(^3P_1):O(^3P_0)$	$(0.51\pm0.09):(0.41\pm0.15):(0.08\pm0.02)$
Dissociation product channel ratios ($\pm 2\sigma$)	
$O(^3P_2)+N_2(A):O(^3P_2)+N_2(B)$	0.71 ± 0.16
$O(^3P_1)+N_2(A):O(^3P_1)+N_2(B)$	0.95 ± 0.06
$O(^3P_0)+N_2(A):O(^3P_0)+N_2(B)$	1.32 ± 0.25
$N_2(A)+O(^3P_J):N_2(B)+O(^3P_J)$	0.84 ± 0.09
$O(^3P)+N_2(A,B):N(^2D,^2P)+NO$	1.4 ± 0.5
$N(^2D_J)+NO:N(^2P_J)+NO$	3

the fine structure levels for $O(^3P_J)$, $N(^2D_J)$, and $N(^2P_J)$. The relative sensitivity for VUV detection of $O(^3P_2)$ and $NO(X,v=0,1)$ at 130.2 nm was established by dissociating NO_2 at 355 nm and was used to calibrate the corresponding O:NO branching ratio obtained from N_2O dissociation.

The composition of the molecular beam was nominally 100% N_2O (99% min, Matheson C.P. grade), except for the experiments detecting the major $O(^1S)$ product channel for which a 10% N_2O mixture in Ar (99.999 5%, Spectra Gases) was prepared. In a diagnostic experiment, a premade 10% NO/ He mixture (9.97%, Matheson) was used. The Krypton was research grade (99.998 5%, Praxair).

RESULTS

Following the dissociation of N_2O at 130.2 nm, the TOF mass spectrum showed product peaks at N^+ or O^+ whenever the ω_2 laser was tuned to the appropriate $(1+1')$ REMPI transition for detection of $N(^2D_J)$, $N(^2P_J)$, $O(^3P_J)$, or $O(^1S)$. Spectral scans over the fine structure levels yielded relative spin-orbit populations for $O(^3P_J)$, $N(^2D_J)$, and $N(^2P_J)$ after normalization for variations in the laser powers. These are given in Table I. Product peaks also were observed for the molecular ions, N_2^+, NO^+, and N_2O^+, due to nonresonant multiphoton ionization processes. Power dependence experiments established that NO^+ was produced by sequential absorption of UV and visible photons by the neutral photoproduct and not by predissociation of N_2O^+. Experiments with a N_2 beam confirmed that N_2^+ could not be produced optically from the ground state, inferring that the signal was due to the ionization of an excited state, likely by VUV absorption. The ratio of mass peaks for O^+ and NO^+ can be converted to the branching ratio between the dissociation channels, leading to $O(^3P)+N_2$ and $N+NO$ by calibrating against the $O^+:NO^+$ mass peak ratio obtained from the dissociation of NO_2 at 355 nm. The ion signals were normalized for variations in laser intensities, using the measured power dependences, and corrected for the fraction of the spin-orbit population appearing as $O(^3P_2)$.[23] The resulting branching ratio is given in Table I.

Velocity-mapped ion images were recorded for the dissociation products of N_2O near 130 nm. The $O+N_2$ product channels are represented by the $O(^1S)$, $O(^3P_2)$, and N_2^+ images in Fig. 1. The $N+NO$ product channels are represented by the $N(^2P_{3/2})$, $N(^2D_{5/2})$, and NO^+ images in Fig. 2. Inverse Abel transformation of the images recovers a slice through the original three-dimensional velocity distribution. Integration over angles yields the speed distributions. The magnification due to the camera lens and ion optics was determined by a calibration of the system with the dissociation of O_2. Conversion to total kinetic-energy released (TKER) allows for comparison between product channels and reveals the internal energy distributions in the unobserved dissociation coproduct. The $O+N_2$ TKER distributions derived from the images in Fig. 1 are shown in Fig. 3. The $O(^3P_0)$ TKER distribution was included to show the effect of the spin-orbit level. Similarly, the $N+NO$ TKER distributions derived from the images in Fig. 2 are shown in Fig. 4. The energy combs in Figs. 3 and 4 were derived from the photon energy, bond energies, and spectral constants.

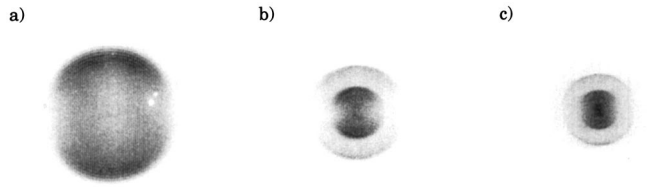

FIG. 1. $O+N_2$ product images from N_2O dissociation at 130.2 nm: (a) $O(^1S)$, (b) $O(^3P_2)$, and (c) N_2^+.

Inspection of the TKER distributions for the $O+N_2$ dissociation channels shows that the observed N_2^+ results from the ionization of N_2 in both the $A\,^3\Sigma^+_u$ and $B\,^3\Pi_g$ electronically excited states, as coproducts with $O(^3P_J)$. $O(^1S)$ is coproduced with unobserved N_2 in the ground electronic state. Electronically excited atoms/diatoms are coupled with ground state diatoms/atoms, respectively. The N_2 $A:B$ branching ratio is easily determined by integration over the two peaks in the O atom TKER, and appears to differ with the atomic fine-structure level. Assuming that the ionization steps are equally efficient, the same information is obtained from the peak areas in the N_2^+ TKER. The $N+NO$ data indicate that the NO^+ image is a composite of two dissociation channels, leading to the two electronically excited states of atomic nitrogen, with the $N(^2P)$ correlating with slower NO and the $N(^2D)$ with faster NO. The $N(^2P)$ products were shown to be bimodal with a minor contribution at very low kinetic energy. The $N(^2D):N(^2P)$ branching ratio may be determined from scaling the TKER distributions from the nitrogen atoms to fit the NO distribution, and accounting for the spin-orbit populations. These branching ratios are also given in Table I. For electronically excited atomic nitrogen and oxygen, the peak kinetic energy is substantially lower

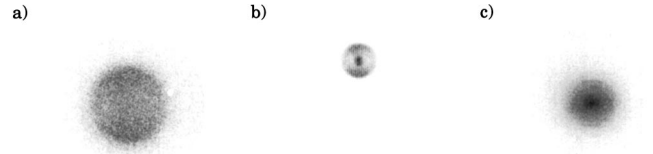

FIG. 2. $N+NO$ product images from N_2O dissociation at 130.2 nm: (a) $N(^2D_{5/2})$, (b) $N(^2P_{3/2})$, and (c) NO^+. The dissociation wavelength for (b) was 131.05 nm.

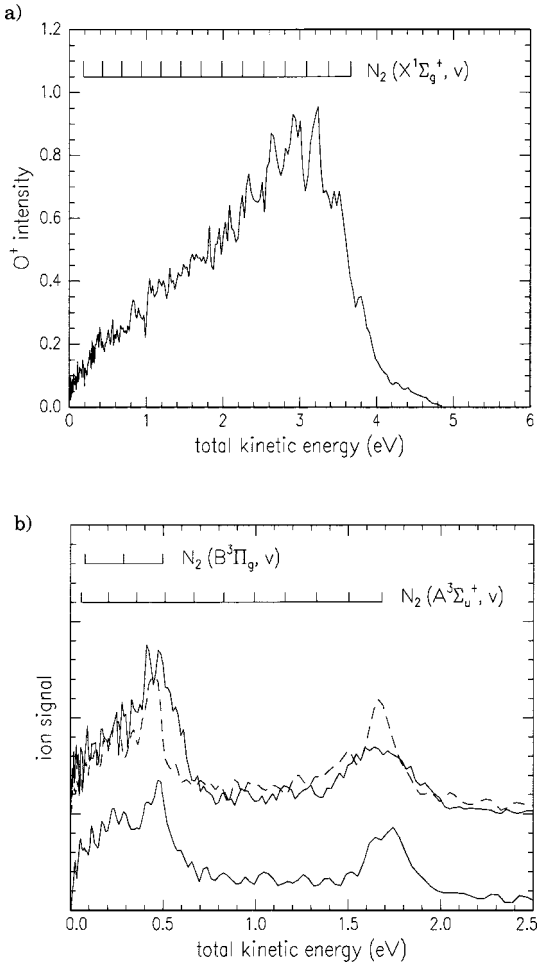

FIG. 3. Total kinetic energy released for $O+N_2$ products from the dissociation of N_2O at 130.2 nm: (a) $O(^1S)$ and (b) $O(^3P_2)$ top solid curver, $O(^3P_0)$ top dashed curve, and N_2^+ bottom curve.

than the maximum allowed by conservation of energy, indicating that the diatoms have significant internal excitation.

Product angular distributions were obtained from the inverse Abel-transformed image by fitting the following function to annuli of eight to ten pixels in width:

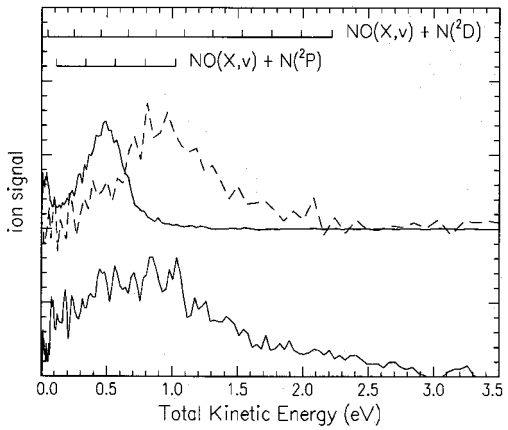

FIG. 4. Total kinetic energy released for N+NO products from the dissociation of N_2O at 130.2 nm: $N(^2P_{3/2})$ top solid curve (at 131.054 nm), $N(^2D_{5/2})$ top dashed curve, and NO^+ bottom curve.

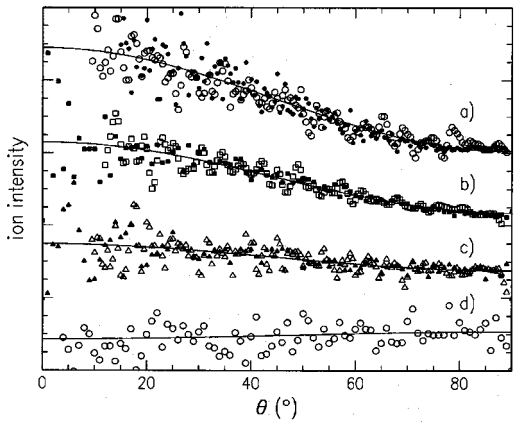

FIG. 5. Angular distributions and fit of $1+\beta P_2(\cos\theta)$: (a) $\beta=1.9$, ● $O(^3P_2)+N_2(A,v=0)$, ○ N_2^+ outer ring; (b) $\beta=1.3$, ■ $O(^1S)+N_2(X,v=0)$, □ $O(^3P_0)+N_2(B,v=0)$; (c) $\beta=0.5$, ▲ $N(^2P_{1/2})+NO(X)$, △ $N(^2D_{5/2})+NO(X)$; and (d) $\beta=-0.14$, ○ NO^+. The zero of the scale is shifted so that all the data can be displayed on one plot.

$$I(\theta) = c[1 + \beta(P_2(\cos\theta)], \tag{9}$$

where c is a scaling constant, β is the anisotropy parameter, which has the limiting values of 2 for a parallel transition and -1 for a perpendicular transition, and $P_2(x)$ is the second-order Legendre polynomial, $1/2\ (3x^2-1)$. For the $O+N_2$ dissociation channels, the fitted anisotropy parameters are large and positive, indicating that the dissociating state is reached by a parallel transition. With increasing vibrational excitation in the N_2 coproduct, however, the anisotropy parameter decreases substantially. The good agreement of the $O(^3P_2)$ and $O(^3P_0)$ angular distributions indicates that there is no alignment of the atomic angular momentum. The N+NO dissociation channels yielded angular distributions for the $N(^2D,^2P)$ products, which are characterized by positive values of β, whereas the NO^+ image appeared to be very nearly isotropic. An alignment of the $N(^2P_J)$ fragments could not be confirmed by comparison of the angular distributions since both $J=1/2$ and $J=3/2$ fragments gave similar β's within the fairly large ($\pm 2\sigma$) uncertainties. Angular distributions together with the resulting fit of Eq. (9) to the data are displayed in Fig. 5, while the determined anisotropy parameters are given in Table II.

DISCUSSION

Branching ratios

A product branching ratio for $O(^3P):NO(X)$ of 1.4 ± 0.5 was obtained for the 130.2-nm dissociation of N_2O. The VUV detection scheme for O and NO was calibrated by using it with the dissociation of NO_2, which has O+NO as the sole product channel. This required the normalization of the O^+ and NO^+ ion signals for variations in the laser powers, using measured power dependences both for N_2O and NO_2 photodissociations. The $O^+:NO^+$ ratio was taken as

$$O^+/NO^+ = (S_O/S_{NO}) f_{SO}[O(^3P)]/[NO],$$

where S_O/S_{NO} is the experimental sensitivity relating the ion signal to number densities, [ ] refers to the number densities, and f_{SO} is the spin-orbit fraction of $O(^3P_J)$ with $J=2$. For the

TABLE II. Anisotropy parameters determined from fitting Eq. (9) to the angular distributions of various N_2O dissociation product channels.

Product channel	Anisotropy parameter $\beta(\pm 2\sigma)$
$O(^1S)+N_2(X,v)$	(v=0) 1.3±0.2; (v=1) 1.3±0.2; (v=2) 1.1±0.1; (v=3) 0.9±0.1
$O(^3P_2)+N_2(A,v)$	(v=0) 2.0±0.2
$O(^3P_0)+N_2(A,v)$	(v=0) 1.8±0.2; (v=1) 1.6±0.3
$N_2(A,v)+O(^3P_J)$	(v=0) 1.8±0.2
$O(^3P_2)+N_2(B,v)$	(v=0) 1.3±0.2; (v=1) 0.7±0.1
$O(^3P_0)+N_2(B,v)$	(v=0) 1.3±0.1; (v=1) 0.9±0.1
$N_2(B,v)+O(^3P_J)$	(v=0) 1.4±0.1; (v=1) 0.9±0.1
$N(^2D_{5/2})+NO(X)$	0.48±0.15
$N(^2P_{3/2})+NO(X)$	0.68±0.12 (fast); 0.03±0.31 (slow)
$N(^2P_{1/2})+NO(X)$	0.51±0.12 (fast); −0.39±0.26 (slow)
$NO(X)+N(^2D^2P)$	−0.14±0.13

dissociation of NO_2 at 355 nm, the relative sensitivity factor is determined because $[O(^3P)]/[NO]$ is unity and f_{SO} has been previously measured to be 0.82.[23] With the relative sensitivity factor known and the spin-orbit fraction measured as 0.51 for N_2O dissociation, the above relationship yields $[O(^3P)]/[NO]$. The $\pm 2\sigma$ uncertainty includes contributions from f_{SO} and the relative ion signals from more than 50 TOF mass spectra recorded at various laser powers. The resulting branching ratio relies on the assumption that the relative sensitivity for O+NO measured with NO (v=0,1) in the NO_2 system does not change significantly over the NO (v=0–9) range of vibrational levels accessible in the N_2O system. That this assumption is reasonable is demonstrated by the good agreement of the TKER distributions of NO^+ with $N(^2D,^2P)$, for which the detection efficiency is independent of the vibrational level of the NO partner.

A product branching ratio for $N(^2D):N(^2P)$ of 3 was obtained for the 130.2-nm dissociation of N_2O from comparison of the TKER distributions of the N atoms with that of NO^+. Beginning with TKER distributions normalized to unit area, the $N(^2D)$ TKER was scaled to fit the NO^+ TKER at energies between 1 and 2 eV. Below 1 eV, $N(^2P)$ begins to make a contribution, especially near 0.5 eV. Scaling the $N(^2P)$ TKER to make up the difference between the results for NO^+ and $N(^2D)$ yields the branching ratio. The sum of the contributions from the N atoms accounts for about 90% of the NO^+ TKER. The regions of mismatch fall in the high-energy wing of the $N(^2D)$ distribution and in the valley of the bimodal $N(^2P)$ distribution (this bimodality appears to be real). It is unlikely that the $NO(v)$ detection efficiency behaves strangely at these particular internal energies. It is more likely that the difficulties in determining and subtracting the background contribution to the weak NO^+ image are the source of the problem. Considering the poor signal-to-noise ratio of both the NO^+ and the $N(^2D)$ TKER distributions, the agreement of the fit is very reasonable. While no uncertainty for the branching ratio is given in Table I, the fit was recognizably worse with $N(^2D)/N(^2P)$ ratios of 2 or 4. The fit assumes that the TKER distributions do not differ between atomic spin-orbit levels. Although this is not the case for $O(^3P_J)$, analysis of $N(^2P_{1/2,3/2})$ images gave insignificantly different TKER distributions. Despite the branching ratio favoring $N(^2D)$ production, the $N(^2P)$ signal was stronger due to the relatively inefficient VUV generation at 124.3 nm compared to 131.05 nm. As well, the ionization step for $N(^2D)$ relied solely on the residual ω_1 ultraviolet laser light, whereas the ionization step for $N(^2P)$ could be effected by the ω_2 visible laser light, which was at least a factor of 5 greater in power.

Product branching ratios for $N_2(A\,^3\Sigma^+_u):N_2(B\,^3\Pi_g)$ were determined from the analysis of the $O(^3P_J)$ and N_2^+ images. The ratio of the integrated peaks in the TKER distributions was on the order of unity, although the ratio did depend strongly on the O atom spin-orbit level detected, favoring the $N_2(A\,^3\Sigma^+_u)$ state for $O(^3P_0)$ and the $N_2(B\,^3\Pi_g)$ state with $O(^3P_{2,1})$. Witinski *et al.* also observed this difference with spin-orbit level and our branching ratio results are in reasonable agreement.[18] The branching ratio obtained from the N_2^+ data incorporates contributions from each of the $O(^3P)$ spin-orbit levels and is consistent with the weighted average (0.86±0.18) of the $O(^3P_{2,1,0})$ branching ratios, where the weights are the measured relative abundances. The good agreement indicates that the ionization efficiencies of the $N_2A\,^3\Sigma^+_u$ and $B\,^3\Pi_g$ states must not be very different at 130.2 nm. As well, the effect of dissociation at $O(^3P_{2,1,0})$ detection wavelengths differing by 0.3 nm is shown to be insignificant.

Previous investigators[3,14] have detected visible $N_2(B^3\Pi_g\text{-}A^3\Sigma^+_u)$ fluorescence, following N_2O dissociation only at shorter wavelengths where the emission is from higher vibrational levels. Their experiments were not sensitive to infrared emission from the low vibrational levels of the B state populated at dissociation wavelengths near 130 nm. As a result, they grossly underestimated the B state population, reporting an $A:B$ branching ratio of 99 at 123.6 nm. Despite the uncertainty in how the relative ionization efficiencies of the two excited electronic states of N_2 change with wavelength, it is clear from the N_2^+ images that the order of magnitude of the A/B ratio is closer to unity than to 100, with values estimated to be 0.3, 0.84, and 3.3 at dissociation wavelengths of 124.3, 130.2, and 131.05 nm, respectively. Because of uncertainties in the relative ionization efficiency mentioned above, we cannot say whether or not there is a systematic trend in the ratio with dissociation wavelength.

Combining the three branching ratios relating $O(^3P)$ to NO, $N(^2P)$ to $N(^2D)$, and $N_2(A\,^3\Sigma^+_u)$ to $N_2(B\,^3\Pi_g)$, the branching between the dissociation channels (5)–(8) at 130.2 nm is

$$O(^3P) + N_2(A\,^3\Sigma^+_u):O(^3P) + N_2(B\,^3\Pi_g):N(^2D) + NO(X\,^2\Pi):N(^2P) + NO(X\,^2\Pi) = 2.6:3:3:1,$$

with $\pm 2\sigma$ uncertainties about 35%. Black *et al.* have determined the $O(^1S)$ quantum yield from N_2O dissociation at 129 nm to be 0.95±0.05 by direct observation of the $O(^1S)$ emission and by comparing the signal level with that from the photodissociation of CO_2 at 112 nm where the quantum yield is unity.[14] They then fixed the quantum yield to be 0.93

because they observed a 0.07 quantum yield for $N_2(A^3\Sigma^+_u)$. Nee *et al.* also measured the $O(^1S)$ quantum yield at dissociation wavelengths close to 130 nm by observing $O(^1S)$ emission enhanced by Xenon buffer gas.[2] From the data in their Fig. 3, the average quantum yield is 0.88 ± 0.05 for wavelengths of 128, 129, 132, and 133 nm. It is reasonable and convenient to fix the $O(^1S)$ quantum yield to be 0.90 at 130.2 nm and to treat our combined branching ratios as % quantum yields. At 130 nm, the quantum yield for $N_2(A^3\Sigma^+_u)$ is given by Black *et al.* as $6\pm1\%$. Under their conditions, the $N_2(B^3\Pi_g)$ would have been completely quenched to $N_2(A^3\Sigma^+_u)$ at the start of the experiment,[24] so that 6% is the sum total of $O(^3P)+N_2(A,B)$. This agrees well with our sum of $2.6\%+3\%$. Their quantum yield of $3\pm3\%$ for $N(^2D)$ at 130 nm is also in agreement with our value. A comparison of our $O(^1S)$ and $O(^3P)$ signal levels after normalizing for laser powers and oscillator strengths for the atomic transitions confirmed the order of magnitude difference in quantum yields for the two electronic states. We cannot give a better estimate without quantifying the relative efficiencies for VUV generation at 121.76 and 130.2 nm and the relative ionization efficiencies of the resonantly excited O atoms.

Vibrational distributions of the N_2 and NO products are qualitatively consistent with the structures of the N_2O excited states determined by Hopper,[17] who found both the N–NO distance and the N–NO distance to be 1.3 Å. Because the N–N distance in the N_2 products is 1.094, 1.293, and 1.2123 Å for the *X*, *A*, and *B* states, respectively,[25] it is clear that the N_2 product will be vibrationally excited for all three channels. Similarly, the N–O bond distance is 1.1508 Å for the NO(*X*) product,[25] so this product also is likely to be vibrationally excited. The vibrational combs in Figs. 3 and 4 provide an indication of the excited vibrational distributions for these diatomic fragments.

Angular distributions

The electronic configuration of the $^1\Sigma^+$ ground state of N_2O is $\ldots(7\sigma)^2(1\pi)^4(2\pi)^4$. *Ab initio* calculations by Hopper[17] have confirmed that the strong absorption near 130 nm is mainly due to the electronic excitation to the linear $\tilde{D}\,^1\Sigma^+$ state the electronic configuration of which is $\ldots(7\sigma)^2(1\pi)^4(2\pi)^3(4\pi)$. The π-π^* excitation weakens both the N–O and the N–N bonds. In addition to the $\tilde{D}\,^1\Sigma^+$ state, there is also a $^3\Pi_v$ state in this same energy region, just slightly higher in energy than the $\tilde{D}\,^1\Sigma^+$ state at the linear geometry. Its electronic configuration is $\ldots(7\sigma)(1\pi)^4(2\pi)^4(3\pi)$, where the last electron is in an antibonding orbital on the N–N and N–O bonds.

Let us first consider the dissociation from these states to N_2+O. For dissociation along the NN–O coordinate, the $\tilde{D}\,^1\Sigma^+$ state correlates in the linear configuration to $N_2(X\,^1\Sigma^+_g)+O(^1S)$, but in the bent configuration it becomes a $^1A'$ state and correlates to $N_2(A\,^3\Sigma^+_u)+O(^3P)$. Thus, there is an avoided seam along the dissociation surface. Along this same NN–O coordinate, the $^3\Pi_v$ state correlates in the linear configuration to $N_2(A\,^3\Sigma^+_u)+O(^3P)$, but in the bent configuration, the $^3\Pi_v$ state becomes two components of a Renner–Teller pair, a lower $^3A'$ state and an upper $^3A''$ state. The lower-energy $^3A'$ component correlates to $N_2(B\,^3\Pi_g)+O(^3P)$, while the higher-energy $^3A''$ component correlates to $N_2(A\,^3\Sigma^+_u)+O(^3P)$. Thus, there is also a seam of crossing between the $^3A'$ and $^3A''$ surface, but this crossing is allowed because the surfaces are of different symmetries. Next, consider the dissociation from the $\tilde{D}\,^1\Sigma^+$ and $^3\Pi_v$ states to N +NO. For dissociation along the N–NO coordinate, the $\tilde{D}\,^1\Sigma^+$ state correlates in the linear configuration to $N(^2P)+NO(X\,^2\Pi)$, and in the bent configuration it correlates to $N(^2D)+NO(X\,^2\Pi)$. Thus, there is another avoided seam along this dissociation surface. Along this N–NO coordinate, the $^3\Pi_v$ state correlates in the linear configuration to $N(^2D)+NO(X\,^2\Pi)$, but in the bent configuration, again, there are two Renner–Teller components. Both the $^3A'$ component and the $^3A''$ component correlate to $N(^2D)+NO(X\,^2\Pi)$. Note that because, in the linear configuration, the $\tilde{D}\,^1\Sigma^+$ state, which is lower in energy than the $^3\Pi_v$ state, correlates to the more energetic $N(^2P)+NO(X\,^2\Pi)$ channel, while the $^3\Pi_v$ state correlates to the less energetic $N(^2D)+NO(X\,^2\Pi)$, there must be a crossing between these surfaces. In the absence of spin-orbit coupling, the crossing is allowed, but in its presence the $^3A'$ and $^1A'$ components may have an avoided crossing.

The angular distributions of the products can help to determine which of these dissociation paths are the most important. In a linear molecule for prompt axial recoil, the expected values of the anisotropy parameter β are, using linearly polarized light, $+2$ for a parallel transition and -1 for a perpendicular transition. For the dissociation of a bent triatomic molecule, again in the axial recoil limit and for linear polarization, the anisotropy parameter is related to the angle α between the recoil direction and the transition dipole moment $\beta=2P_2(\cos\alpha)$, where $P_2(\,)$ is the second Legendre polynomial.

We now enumerate the various product channels, note how each may be reached, and comment on the expected and measured anisotropy parameters. The $N_2(X\,^1\Sigma^+_g)+O(^1S)$ channel is accessed by dissociation only from the $\tilde{D}\,^1\Sigma^+$ state in the linear configuration. For a parallel transition, such as from the N_2O ground state $\tilde{X}\,^1\Sigma^+$ to the optically allowed $\tilde{D}\,^1\Sigma^+$ state, the limiting value of the anisotropy parameter β is well-known to be $+2$ for dissociation by linearly polarized light or -1 for dissociation by unpolarized light.[26] The angular distribution of the $O(^1S)$ fragment from the 130-nm photodissociation measured by Stone *et al.* using an unpolarized light source is consistent with $\beta=-1$, indicating a parallel transition.[16] Similarly, our own measurement using linearly polarized light gave $\beta=1.3$ for the $O(^1S)$, consistent with a parallel transition, but perhaps not quite as high as we might have expected.

The $N_2(A\,^3\Sigma^+_u)+O(^3P)$ channel is accessed (a) from the $\tilde{D}\,^1\Sigma^+$ state after it bends to become $^1A'$, (b) from the $^3\Pi_v$ state in the linear configuration, or (c) from the upper $^3A''$ Renner–Teller component of the $^3\Pi_v$ state in the bent configuration. The basic transition is again a parallel one, but two of the three possibilities come from dissociation of a bent N_2O. Thus, we might expect that β could be reduced from its limiting value of 2.0. Somewhat surprisingly, the

data indicate $\beta=2.0$, so that it must be that dissociation takes place from a nearly linear configuration. The correlations calculated by Hopper would suggest that dissociation proceeds following crossing to the $^3\Pi_v$ state.

The $N_2(B\,^3\Pi_g)+O(^3P)$ channel can come only from the lower $^3A'$ component of the $^3\Pi_v$, state in the bent configuration (assuming that only the $\tilde{D}\,^1\Sigma^+$ and $^3\Pi_v$ states to be involved). The data indicate that $\beta=1.3$, in general agreement with a parallel excitation followed by dissociation from a somewhat bent geometry. Witinski *et al.* also reported a similar value of $\beta=1.5$ for this channel.[18]

The $N(^2D)+NO(X\,^2\Pi)$ channel can come (a) from the $^3\Pi_v$ state in a linear configuration, (b) from either of the Renner–Teller components of the $^3\Pi_v$ state in a bent configuration, or (c) from the bent ($^1A'$) configuration of the $\tilde{D}\,^1\Sigma^+$ state. The $N(^2D)$ image gives a β of 0.5, suggesting that the bent configurations dominate.

Finally, the $N(^2P)+NO(X^2\Pi)$ channel comes only from the linear configuration of the $\tilde{D}^1\Sigma^+$ state. We expect $\beta=2$, but the data suggest something lower, $\beta=0.5$–0.7. The value of the anisotropy parameter, based on measurement of the $NO(X\,^2\Pi)$ channel, is also somewhat lower than expected from the measured parameters for the $N(^2P)$ and $N(^2D)$, but this determination is rendered less certain due to the necessity for background subtraction in the measurement.

The variations of the anisotropy parameter β with internal energy of the diatomic fragment indicated in Table I can be understood qualitatively based on the model described by Demyanenko *et al.*[27] in which the transverse recoil component is calculated based on the angular momentum calculation. The principal result is given by the equation

$$\sin^2\phi=\frac{\mu_{\text{diatom}}r^2}{\mu_{A-BC}R_C^2\left(\dfrac{E_{\text{avl}}}{E_{\text{rot}}}-1\right)},$$

where ϕ is the angle between the actual and axial recoil directions, $E_{\text{avl}}=E_{\text{trans}}+E_{\text{rot}}$ is the energy available to the fragments, exclusive of internal vibrational and electronic energy, r is the diatomic bond length, and R_c is a critical distance parameter at which the angular momenta have reached their final values. Because we do not resolve the rotational energy of the fragment, we cannot perform a quantitative analysis, but it is clear from the formula that as E_{avl} decreases, assuming comparably sampled values for E_{rot}, the denominator will decrease, leading to larger predictions for ϕ. Because, in this theory, $\beta=2P_2(\cos(\alpha\pm\phi))$, it is clear that β should decrease with decreasing E_{avl}. This behavior is observed for the $O(^1S)+N_2(X,v)$ channel, the $O(^3P_0)+N_2(A,v)$ channel, the $O+N_2(B,v)$ channel, and the $N(^2P)+NO(X)$ channels.

CONCLUSIONS

Dissociation of N_2O near 130 nm leads to at least five product channels, (4)–(8). Based on this and previous work, it appears that channel (4) dominates, with minor contributions from (5)–(8), all of the quantum yields between 1% and 3%. Both of the diatomic products are vibrationally excited in all accessible channels. The spin-orbit ratios, relative branching ratios, and anisotropy parameters have been determined, as listed in Tables I and II. The dynamics of the dissociation appear to be consistent with the calculations of Hopper; dissociation takes place predominantly through the $\tilde{D}^1\Sigma^+$ state, with likely participation of the $^3\Pi_v$ state.

ACKNOWLEDGMENTS

This work was supported by the Department of Energy under Grant No. DE-FG02-88ER13934 and in part by the National Science Foundation under Grant No. CHE-0239903. We have benefitted from conversations with M. F. Witinski, M. Ortiz-suárez, and H. F. Davic, who are thanked for making a copy of their paper available to us prior to publication.

[1] P. J. Crutzen, Q. J. R. Meteorol. Soc. **96**, 320 (1970); P. J. Crutzen, J. Geophys. Res. **76**, 7311 (1971).
[2] J. B. Nee, J. C. Yang, P. C. Lee, X. Y. Wang, and C. T. Juo, Chin. J. Phys. (Taipei) **37**, 172 (1999).
[3] L. C. Lee and M. Suto, J. Chem. Phys. **80**, 4718 (1984).
[4] M. Zelikoff, K. Watanabe, and E. C. Y. Inn, J. Chem. Phys. **21** 1643 (1953).
[5] P. Felder, B.-M. Haas, and J. R. Huber, Chem. Phys. Lett. **186**, 177 (1991).
[6] N. Shafer, K. Tonokura, Y. Matsumi, S. Tasaki, and M. Kawasaki, J. Chem. Phys. **95**, 6218 (1991).
[7] L. L. Springsteen, S. Satyapal, Y. Matsumi, L. M. Dobeck, and P. L. Houston, J. Phys. Chem. **97**, 7239 (1993).
[8] T. F. Hanisco and A. C. Kummel, J. Phys. Chem. **97**, 7242 (1993).
[9] T. Suzuki, H. Katayanagi, Y. Mo, and K. Tonokura, Chem. Phys. Lett. **256**, 90 (1996).
[10] D. W. Neyer, A. J. R. Heck, and D. W. Chandler, J. Chem. Phys. **110**, 3411 (1999).
[11] D. W. Neyer, A. J. R. Heck, D. W. Chandler, J. M. Teule, and M. H. M. Janssen, J. Phys. Chem. A **103**, 10388 (1999).
[12] A. Brown, P. Jimeno, and G. G. Balint-Kurti, J. Phys. Chem. A **103**, 11089 (1999).
[13] S. Nishida, K. Takahashi, Y. Matsumi, N. Taniguchi, and S. Hayashida, J. Phys. Chem. A **108**, 2451 (2004).
[14] G. Black, R. L. Sharpless, T. G. Slanger, and D. C. Lorents, J. Chem. Phys. **62**, 4266 (1975).
[15] R. Gilpin and K. H. Welge, J. Chem. Phys. **55**, 975 (1971)
[16] E. J. Stone, G. M. Lawrence, and C. E. Fairchild, J. Chem. Phys. **65**, 5083 (1976).
[17] D. G. Hopper, J. Chem. Phys. **80**, 4290 (1984).
[18] M. F. Witinski, M. Ortiz-Suárez and H. F. Davis, J. Chem. Phys. **122**, 174303 (2005), preceding paper.
[19] R. J. Wilson, J. A. Mueller, and P. L. Houston, J. Phys. Chem. A **101**, 7593 (1997).
[20] B.-Y. Chang, R. C. Hoetzlein, J. A. Mueller, J. D. Geiser, and P. L. Houston, Rev. Sci. Instrum. **69**, 1665 (1998).
[21] B. R. Cosofret, H. M. Lambert, and P. L. Houston, J. Chem. Phys. **117**, 8787 (2002).
[22] H. M. Lambert, A. A. Dixit, E. W. Davis, and P. L. Houston, J. Chem. Phys. **121**, 10437 (2004).
[23] J. Miyawaki, T. Tsuchizawa, K. Yamanouchi, and S. Tsuchiya, Chem. Phys. Lett. **165**, 168 (1990).
[24] R. A. Young, G. Black, and T. G. Slanger, J. Chem. Phys. **50**, 303 (1969).
[25] G. Herzberg, *Spectra of Diatomic Molecules* (Van Nostrand, New York, 1950).
[26] R. N. Zare, Mol. Photochem. **4**, 1 (1972).
[27] A. B. Demyanenko, B. Dribinski, H. Reisler, H. Meyer, and C. X. W. Qian, J. Chem. Phys. **111**, 7384 (1999).